Supplementary Material

Faster hemodynamic signals observed in low-intensity and high-resolution fMRI studies

Jingyuan E. Chen[a,b], Gary H. Glover[c], Nina E. Fultz[a], Bruce R. Rosen[a,b,d], Jonathan R. Polimeni[a,b,d] , Laura D. Lewis[e]

[a] Athinoula A. Martinos Center for Biomedical Imaging, Massachusetts General Hospital, Boston, MA, USA

[b] Department of Radiology, Harvard Medical School, Boston, MA, USA

[c] Department of Radiology, Stanford University, Stanford, CA, USA

[d] Harvard-Massachusetts Institute of Technology Division of Health Sciences and Technology, Cambridge, MA, USA

[e] Department of Biomedical Engineering, Boston University, Boston, MA, USA

Table S1 Summary of subject participation in the flickering checkerboard experiments with two graded luminance levels (section 2.1.1 in the main text). 'X' marks the data included for reports. A total of 10 subjects participated in this experiment and underwent simultaneous EEG/fMRI scans of 6-s visual stimuli. Among whom, the fMRI data of 1 subject were not successfully collected; the EEG data of a few subjects demonstrated no clear SSVEP (clear narrow peaks at the checkerboard flickering frequency) or alpha activity in the neural electrodes (see below, with no 'X'), and were hence excluded for ensuing characterization of contrast-dependent modulation. A subset of 6 subjects returned for another fMRI-only experiment that consisted of 1-s visual stimuli.

Subject Index	6-s trials (EEG/fMRI)			1-s trials (fMRI)
	fMRI	SSVEP	alpha	
01	X			X
02	X			
03	X	X	X	X
04	X		X	X
05	X		X	X
06		X	X	
07	X	X	X	
08	X	X	X	X
09	X	X	X	
10	X	X	X	X
11	X			
12	X			
13	X			
14	X			X
15	X			
# of trials (mean$\pm$stdev across subjects)	'High': 51$\pm$17 'Low': 79$\pm$26	'High': 72$\pm$23 'Low':113$\pm$36	'High': 57$\pm$28 'Low': 90$\pm$44	'High': 69$\pm$17 'Low': 108$\pm$26

SM 1 Modelling contrast-dependent HRF patterns based on EEG measurements

Model I: Forward biophysical modeling of BOLD dynamics predicted by SSVEP/alpha wave activity.

Neurovascular coupling: Neurally-driven CBF changes $f(t)$ were simulated by linearly convolving task-evoked SSVEP or alpha patterns $N(t)$ with a Gamma-variate function $h(t)$ as follows:

$$h(t) = \frac{1}{k\tau_h(k-1)!}\left(\frac{t}{\tau_h}\right)^k e^{-t/\tau_h}$$
$$f(t) = 1 + k_f h(t-\delta_{tf}) * N(t) \qquad \text{eqn. (1)}$$

where $k = 3, \tau_h = 0.968$ s (corresponding to a FWHM of 4 s for $h(t)$), the temporal delay in CBF $\delta_{tf} = 1$ s. k_f is the scaling factor that normalizes $f(t)$ —with $k_f^{1.8\%,SSVEP} = 7.7, k_f^{30\%,SSVEP} = 11, k_f^{1.8\%,alpha} = 0.086, k_f^{30\%,alpha} = 0.17$, the simulated BOLD percent signal change (PSC) is 1.6% for the lower luminance level and 4% for the higher luminance level. Note that we have scaled

down the PSC in contrast to the empirical observation in Fig. 1B (~4% for the lower luminance level and 10% for the higher luminance level), in order to approach the PSC level conventionally modeled under the balloon model; this compatibility can be alternatively achieved by altering the dimensionless parameters that define intra- and extra-vascular BOLD contributions in eqn. (5) below.

Flow-volume dynamics (the balloon model): The transformation of CBF to BOLD dynamics follows the balloon model [cite], with the volume of the balloon $v(t)$ and the total deoxyhemoglobin $q(t)$ simulated as:

$$\dot{q}(t) = \frac{1}{\tau_{MTT}}\left[m(t) - \frac{q(t)}{v(t)} f_{out}(v,t)\right]$$
$$\dot{v}(t) = \frac{1}{\tau_{MTT}}[f(t) - f_{out}(v,t)] \qquad \text{eqn. (2)}$$

where $\tau_{MTT} = 2$ s is the mean transit time through the balloon (the ratio of the resting-state blood volume to blood flow), and $\tau_v = 30\ s$ is the viscoelastic time constant of the rapid volume change (identical values are used for inflation and deflation). The $CMRO_2$ response $m(t)$ is modeled via $f(t)$ by a coupling ratio n and a temporal delay $\delta_{tm} = 1$ s:

$$m(t) = 1 + \frac{f(t - \delta_{tm}) - 1}{n} \qquad \text{eqn. (3)}$$

The output flow is additionally modeled as:

$$f_{out}(v,t) = \frac{1}{\tau_v + \tau_{MTT}} \tau_{MTT} v(t)^{1/\alpha} + \tau_v f(t) \qquad \text{eqn. (4)}$$

with the steady-state flow-volume coupling ratio $\alpha = 0.4$.

BOLD percent signal change takes the following form:

$$\frac{\Delta S}{S} = V_0 \left[k_1(1-q) + k_2\left(1 - \frac{q}{v}\right) + k_3(1-v)\right] \qquad \text{eqn. (5)}$$

where baseline blood volume $V_0 = 0.03$, dimensionless parameters $k_1 = 6.7$, $k_2 = 2.73$, and $k_3 = 0.57$.

Model II: Impulse HRFs responsive to 1.8% and 30% contrast levels.

Impulse HRF changes were characterized under a linear regression paradigm illustrated in Fig. S1 below. The set of bases functions (v) introduced in **SM3** were employed for $iHRF(t)$ fitting.

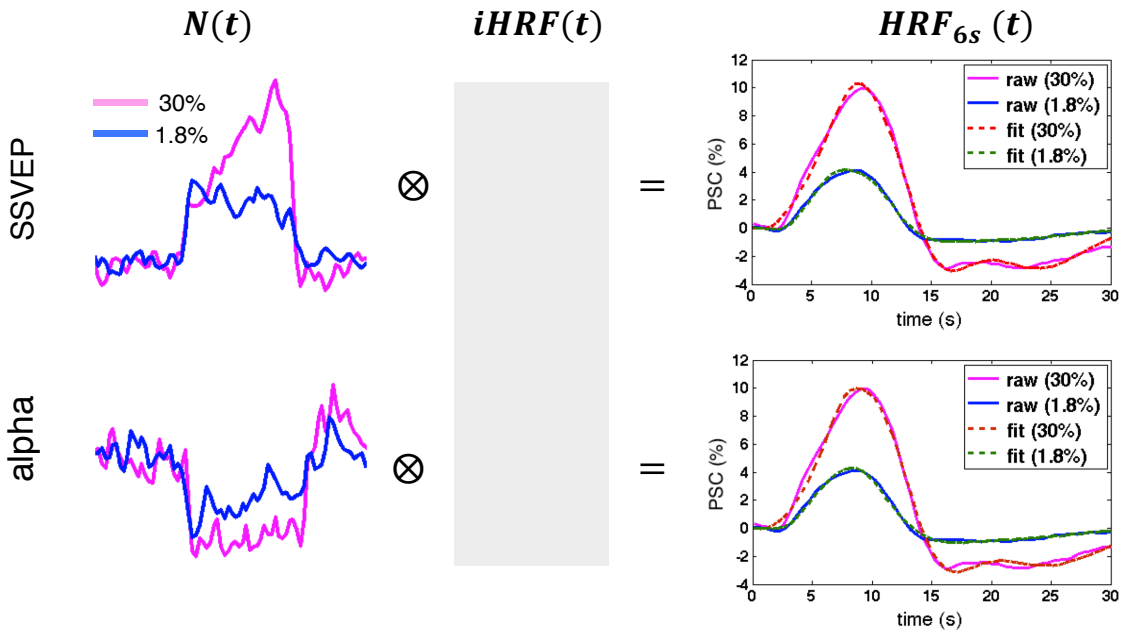

Fig. S1 Illustration of waveforms included in the regression model. $N(t)$: mean SSVEP/alpha envelope of all subjects (Fig. 4); $HRF_{6s}(t)$: mean HRFs ('raw') elicited by 6-s task trials across all subjects (Fig. 1B) and fitted curves ('fit') by the HRF basis (v).

SM2 Influence of selected HRF bases on quantified dispersion of TTPs, FWHMs and frequency responses of voxel-wise HRFs (section 2.2.4 of the main text)

To alleviate the bias of specific HRF basis functions, we evaluated the fMRI results with five different sets of HRF bases:
(i) The canonical SPM HRF with its temporal and dispersive derivatives (3 functions);
(ii) Three Gamma-variate functions;
(iii) The first 3 principal components of HRF functions constructed following the FSL FLOBS concept (the ranges of parameters are listed below):
(iv) The first 6 principal components of HRF functions constructed following the FLOBS approach.

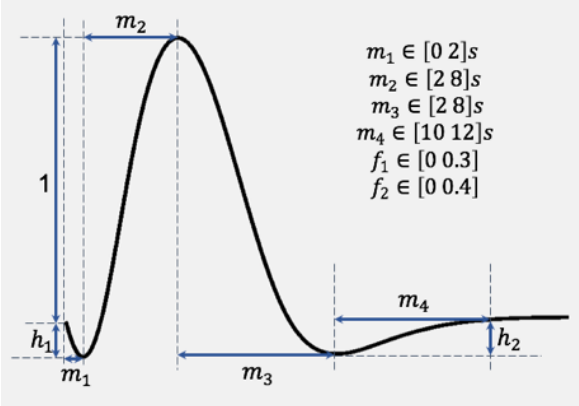

(v) The canonical SPM HRF (eqn. 6) and its derivatives with respect to a, b, c, d, k:

$$mHrf(t) = \frac{1}{\Gamma(a)b^a} t^{a-1} e^{-\frac{t}{b}} - \frac{k}{\Gamma(c)d^c} t^{c-1} e^{-\frac{t}{d}} \qquad \text{eqn. (6)}$$

with $a = 6, b = 1, c = 16, d = 1, k = 1/6$.

As shown in Fig. S2 below, although the specific ranges of quantified HRF features varied across different basis functions, remarkable inter-voxel variability of TTPs, FWHMs and $A_{0.2}/A_{0.1}$, as well as the negative influence of effective voxel size on HRF variability was consistently observed, suggesting that our findings were not biased by the specific HRF bases we chose. We reported the basis set (v) in the main text, because it resulted in the best fitting results when inspecting individual voxel's time series (not shown).

Figure S2 Dispersions of voxel-wise TTPs, FWHMs and $A_{0.2}/A_{0.1}$, and the influence exerted by spatial smoothing (each column shows the results fitted by one set of HRF bases).

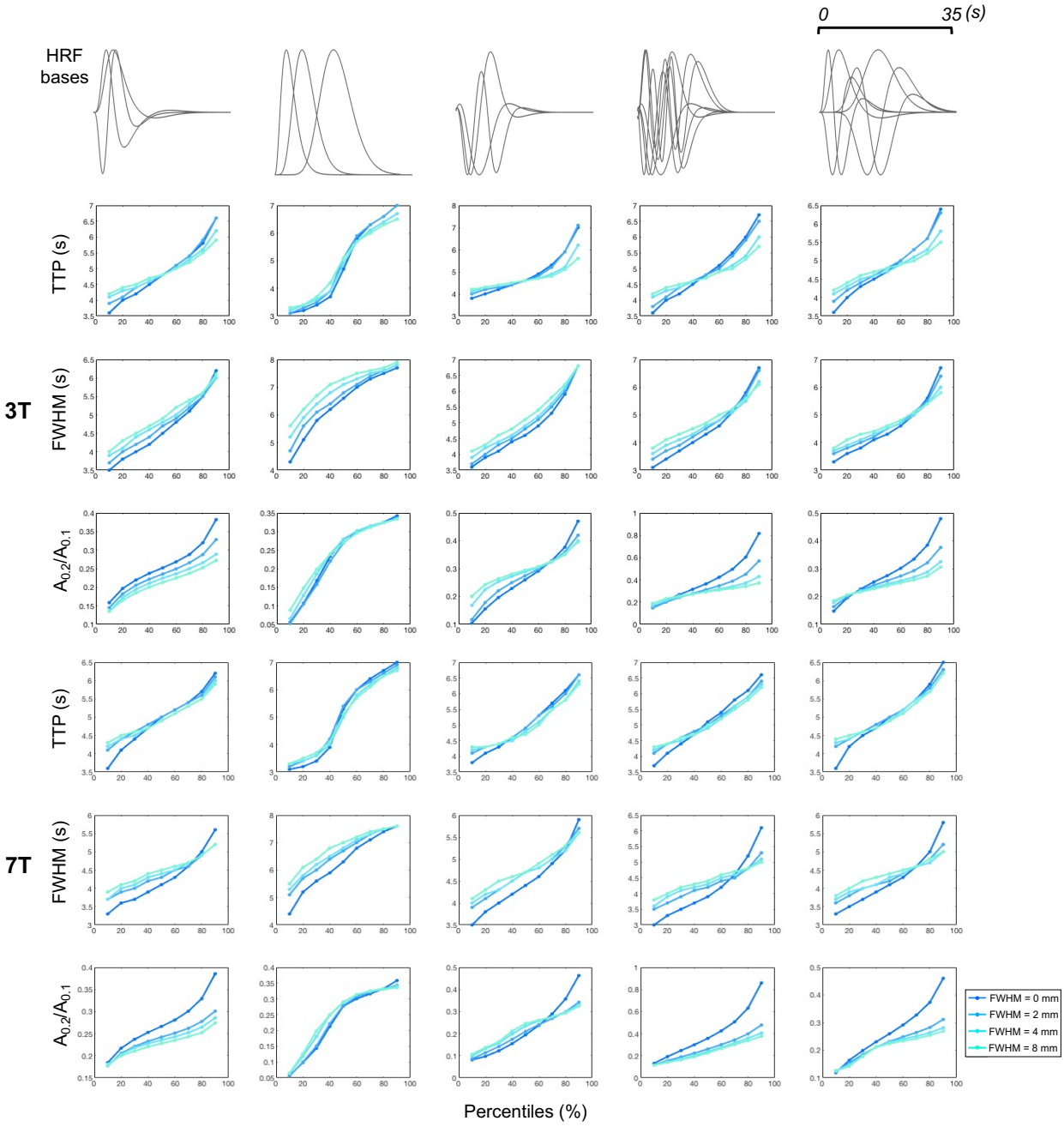

SM 3 Subject-level results of contrast-dependent sensorimotor HRFs

Figure S3 Subject-level HRFs evoked by graded vibrotactile stimuli (mean and standard errors across trials). The mean HRF of voxels within a left postcentral gyrus region of interest (bottom right, derived by projecting the group-level activation map to each subject's native image space) is displayed; and the black curve in each panel shows the response modeled by the SPM canonical function (scaled to match the peak percent signal change induced by the highest contrast). Indexes of individual results included for reports in Fig. 2B are highlighted in purple.

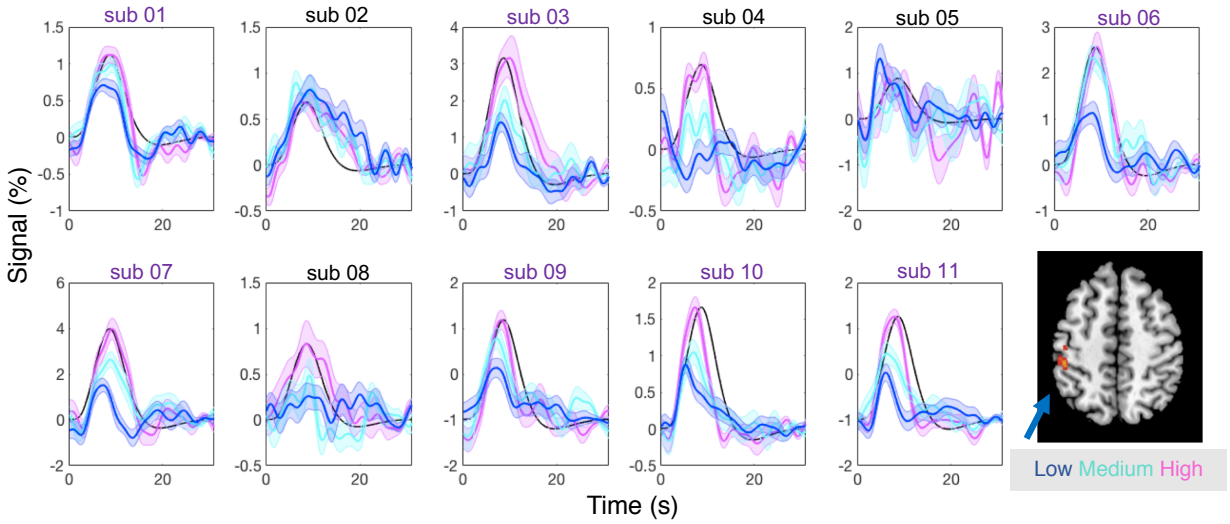

SM 4 Potential vascular mechanisms underlying contrast-dependent HRF changes.

The biophysical model (*Model I*) described in SM1 was used to simulate the influence of contrast-dependent neurovascular and flow-volume coupling patterns on resultant HRF changes. As shown in Fig. S4 below, these vascular aspects can also account for diminished PSUs in lower-contrast HRFs, and narrower FWHMs that cannot be explained by the EEG signatures, suggesting that contrast-dependent hemodynamic patterns may arise partly from vascular mechanisms.

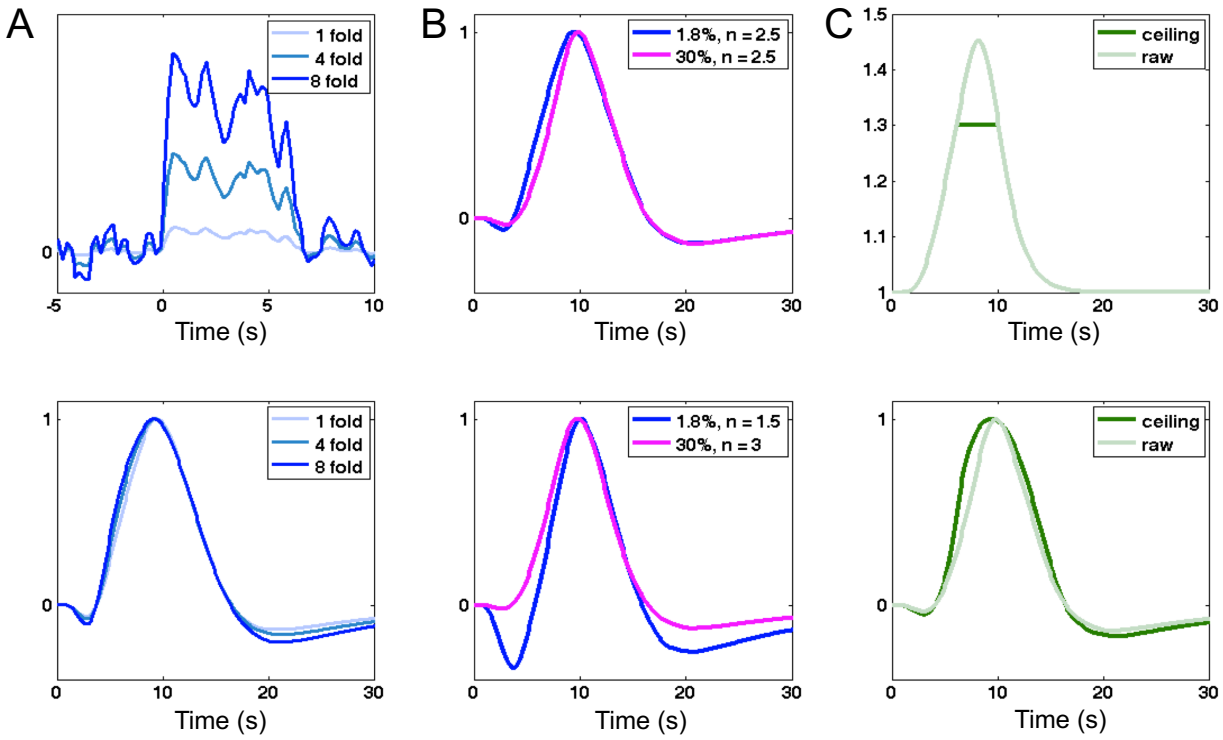

Figure S4 (A) Influence of contrast-dependent flow-volume coupling was simulated by scaling the envelope of $SSVEP_{1.8\%}$ (proportionally, the CBF changes) with varying folds; smaller task intensity corresponds to narrower FWHMs and diminished PSUs; (B) Smaller flow-metabolism coupling ratio associated with the lower task contrast predicts a narrower FWHM; (C) CBF ceiling effects can yield apparently wider FWHMs. All simulated HRFs are normalized by their maximum intensities for comparisons.

SM 5 Acquisition and experiments of the data presented in Fig. 6.

Acquisition: MR images were collected on a 3T Siemens Trio scanner with a vendor-supplied 32-channel head coil. *High-resolution angiography:* A multi-gradient echo acquisition was used to derive the angiography information (voxel size $0.5 \times 0.5 \times 1.7$ mm, TR = 315 ms, TE = 4.05/9.54/15.03/20.52/26.01/31.50/36.99/42.48/47.97/53.46 ms, flip angle = 60^o, FOV = 120×120 mm, single slice, bandwidth = 300 Hz/Pixel). Images of the first two echoes (with the highest inflow contrasts) were averaged, yielding the angiography map shown in Fig. 6A. *Functional images*: A standard inter-leaved multi-slice EPI (voxel size = 1.5×1.5×1.7 mm, TR = 530 ms, TE = 30 ms, flip angle = 53^o, FOV = 120×105 mm, 7 slices with no gap and the middle slice aligned to the angiography plane, phase partial Fourier factor = 7/8, echo spacing = 0.76 ms, bandwidth = 1562 Hz/Pixel) was used to map brain functional changes.

Experiments: One subject participated in the block-design visual experiment (task 'on': radial checkerboard flickering at 12 Hz; task 'off': gray background). The experiment consists of three sessions, with five blocks per session, 25-s on and 35-s off per block. To achieve accurate registration between the angiography and EPI data, a customized head case (https://caseforge.co) was employed to minimize head motion.

SM 6 Assessing the influence of white noise levels on estimated HRF variability

To minimize the potential contamination from white noise, HRF fitting performed in Experiment 2 was based on the mean fMRI time course across multiple sessions and very stringent statistical thresholds were chosen to include voxels demonstrating evident task effects. To further test whether the amplified HRF variability at higher spatial resolutions (Fig. 5 of the main text) mirrored the intrinsic heterogeneity of HRFs instead of noisier HRF fitting, we performed additional simulations. Briefly, we generated a set of sham datasets following the scheme outlined in **Figure S5**. The sham datasets had identical HRF distributions as the low-resolution fMRI data (post 3D spatial smoothing, FWHM = 8 mm), and comparable noise levels as the high-resolution fMRI data (without spatial smoothing). We then quantified and compared the HRF speed measures derived from the high-resolution fMRI data and those "sham" datasets, to test whether our observations in Fig. 5 were dominated by noise. The results are summarized in **Table S2**. Overall, the measured HRF variability of the raw high-resolution data was greater than that caused by noise, suggesting that our characterizations were not dominated by noise.

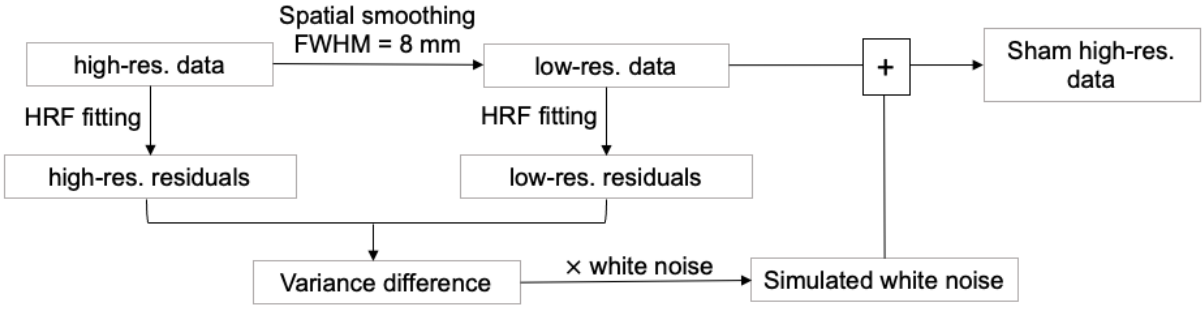

Figure S5 The scheme of generating the "sham" high-res fMRI data based on a single-session fMRI data. The simulated "sham" dataset had identical noise levels as the raw high-resolution fMRI data ("high-res. data"), and consistent HRF distributions as the spatially-smoothed (3D isotropic Gaussian kernel FWHM = 8 mm) low-resolution data ("low-res. data"). To construct the null distributions of group-level HRF speed metrics (**Table S2** below), the "sham" dataset was generated for every single-session dataset of each subject, and 500 group-level "sham" datasets were simulated.

Table S2 Summary of HRF speed measures: raw vs. "sham" high-res fMRI data. TTP, FWHM and $A_{0.2}/A_{0.1}$were defined in section 2.2.4 of the main text. 'TTP faster/slower': mean HRF across top/bottom 20% voxels demonstrating faster/slower TTPs; 'FWHM faster/slower': mean HRF across top/bottom 20% voxels demonstrating narrower/broader FWHMs; '$A_{0.2}/A_{0.1}$ faster/slower': mean HRF across top/bottom 20% voxels demonstrating larger/smaller $A_{0.2}/A_{0.1}$ values. Overall, the empirical measurements ('raw') exhibited greater variability than simulated sham data (95% confidence intervals were shown), contrasting the faster/slower values with the 95% CIs.

HRF features		3 T		7 T	
		raw	95% CI	raw	95% CI
TTP (s)	faster	3.4	[4.1 4.2]	3.5	[4.5 4.6]
	slower	6.4	[5.6 5.9]	6.6	[5.5 5.6]
FWHM (s)	faster	3.4	[3.7 3.9]	3.3	[4.1 4.3]
	slower	6.8	[5.8 6.5]	6.1	[4.8 4.9]

$A_{0.2}/A_{0.1}$	slower	0.10	[0.14 0.20]	0.07	[0.13 0.14]
	faster	0.34	[0.28 0.32]	0.34	[0.22 0.24]